High-resolution pseudo-inverse ghost imaging

Wenlin Gong

Key Laboratory for Quantum Optics and Center for Cold Atom Physics of CAS, Shanghai Institute of Optics and Fine Mechanics, Chinese Academy of Sciences, Shanghai 201800, China (gongwl@siom.ac.cn)

Received June 19, 2015; revised July 21, 2015; accepted July 21, 2015;
posted July 23, 2015 (Doc. ID 243400); published August 21, 2015

We present a pseudo-inverse ghost imaging (PGI) technique which can dramatically enhance the spatial transverse resolution of pseudo-thermal ghost imaging (GI). In comparison with conventional GI, PGI can break the limitation on the imaging resolution imposed by the speckle's transverse size on the object plane and also enables the reconstruction of an N-pixel image from much less than N measurements. This feature also allows high-resolution imaging of gray-scale objects. Experimental and numerical data assessing the performance of the technique are presented.

OCIS codes: (270.0270) Quantum optics; (110.2990) Image formation theory; (100.3010) Image reconstruction techniques; (030.6140) Speckle.
http://dx.doi.org/10.1364/PRJ.3.000234

1. INTRODUCTION

Ghost imaging (GI), which is based on the quantum or classical correlation of fluctuating light fields, has been demonstrated theoretically and experimentally to show that an unknown object can be nonlocally imaged without being scanned by using a single-pixel detector at the object path [1–10]. Because all the photons reflected (or transmitted) from the object illuminate the same single-pixel detector, this technique has the capability of being highly sensitive in detection and offers great potentialities with respect to standard conventional imaging [11–15]. For example, the dosage of fluorescence protein used for GI can be dramatically reduced compared with modern fluorescence-imaging methods in biomedical imaging, and the imaging in the wavebands without cameras can be achieved with a single pixel detector. Other potentialities are in the direction of high efficiency in information extraction, where an N-pixel image can be reconstructed from less than N measurements because the measurement mechanism of GI is random and global [8,16,17]. Due to these remarkable features, GI has been gradually applied to biomedical imaging [12,13], remote sensing [14,15], optical encryption [18], secure key distribution [19], and so on. However, the spatial resolution of GI is limited by the speckle's transverse size on the object plane, and improving its spatial transverse resolution becomes a key issue [5,9,20,21]. When the object's sparsity has been taken as *a priori*, ghost imaging via sparsity constraint (GISC) has been experimentally demonstrated to show that the spatial transverse resolution of GI can be enhanced for simple binary objects (transmission 0 or 1), but the reconstruction time is much longer than the conventional GI method and the high-resolution capability for a low-contrast object or gray-scale object has not been reported [20,21]. Even if GISC can improve the imaging resolution of low-contrast or gray-scale objects, the improvement degree of imaging resolution may be limited because these objects are not sparse. In real sensing and imaging applications, the object is usually gray-scale. Therefore, in order to promote and expand the practical applications of GI, it is imperative to develop a universal and real-time high-resolution GI method for gray-scale objects. Recently, the object's ghost image has been reconstructed by a pseudo-inverse method, and the measurement number required for reconstructing GI with a good signal-to-noise ratio is on the same order of magnitude as GISC [22]. However, the object's sparsity is not utilized. Based on the property of the pseudo-inverse matrix, it is possible to enhance the spatial resolution of GI. In this article, we present a pseudo-inverse ghost imaging (PGI) method that dramatically improves the spatial transverse resolution of GI and reconstructs an N-pixel image from much less than N measurements even for gray-scale objects. Based on previous GI research achievements, PGI further paves the way for real applications of the GI protocol, with the possibility of exploiting all the advantages of GI against standard conventional imaging.

2. EXPERIMENTAL SETUP AND IMAGE RECONSTRUCTION

To demonstrate high-resolution PGI, we constructed the setup illustrated in Fig. 1. The pseudo-thermal light source, which is obtained by passing a collimated laser beam (with wavelength $\lambda = 650$ nm and the source's transverse size $D = 4.0$ mm) through a slowly rotating ground glass disk [7,17], goes successively through a hole with diameter $D_0 = 8.0$ mm and a lens f, and then is divided by a beam splitter into object and reference paths. In the object path, the light goes through a transmission object O and its transmitted image is imaged onto a bucket detector D_t by a standard conventional imaging setup. In the reference path, the light propagates directly to a CCD camera D_r. Both the camera D_r and the object are placed on the conjugate plane of the hole.

In the framework of conventional GI, the object's image $O_{\mathrm{GI}}(x, y)$ can be reconstructed by computing the intensity correlation between the speckle's intensity distributions $I_r^s(x, y)$ recorded by the CCD camera D_r and the total intensities B^s recorded by the bucket detector D_t [8,9],

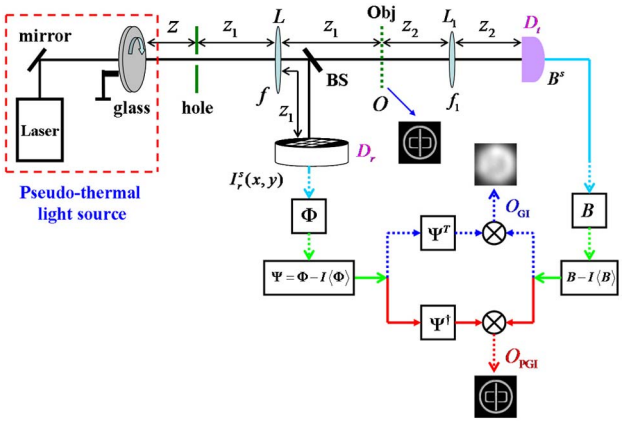

Fig. 1. Experimental schematic of PGI with pseudo-thermal light. The blue dashed line and the red solid line in the bottom right of the schematic correspond to the GI reconstruction method ($O_{\mathrm{GI}} = \Psi^T(B - I\langle B\rangle)$) and PGI reconstruction method ($O_{\mathrm{PGI}} = \Psi^\dagger(B - I\langle B\rangle)$), respectively.

$$O_{\mathrm{GI}}(x,y) = \frac{1}{K}\sum_{s=1}^{K} I_r^s(x,y)(B^s - \langle B^s\rangle) = \frac{1}{K}\sum_{s=1}^{K}(I_r^s(x,y) - \langle I_r^s(x,y)\rangle)(B^s - \langle B^s\rangle). \quad (1)$$

Here, s denotes the sth measurement and K is the total measurement number. In addition, when the numerical aperture of the lens f_1 shown in Fig. 1 is large enough, $B^s = \int \mathrm{d}x\mathrm{d}y I_t^s(x,y)O(x,y)$ (where $O(x,y)$ is the object's transmission function) and we set $I_t^s(x,y) = \alpha I_r^s(x,y)$, where α is a factor which takes into account any unbalancing (beam splitter and detectors) between the two paths. $\langle B^s\rangle = \frac{1}{K}\Sigma_{s=1}^{K} B^s$ and $\langle I_r^s(x,y)\rangle = \frac{1}{K}\Sigma_{s=1}^{K} I_r^s(x,y)$ represent the ensemble average of B^s and $I_r^s(x,y)$, respectively.

Obviously, as shown in Fig. 1, Eq. (1) can be expressed as a series of matrix operations. Provided that each of the speckle's intensity distributions $I_r^s(x,y)$ is an $m \times n$ image and the object O is also an $m \times n$ image, then

$$O_{\mathrm{GI}} = \frac{1}{K}(\Phi - I\langle\Phi\rangle)^T(B - I\langle B\rangle). \quad (2)$$

Here, Φ is a $K \times N (N = m \times n)$ matrix and Φ^T denotes the transposition of the matrix Φ, namely

$$\Phi = \begin{bmatrix} I_r^1(1,1) & I_r^1(1,2) & \cdots & I_r^1(m,n) \\ I_r^2(1,1) & I_r^2(1,2) & \cdots & I_r^2(m,n) \\ \vdots & \vdots & \ddots & \vdots \\ I_r^s(1,1) & I_r^s(1,2) & \cdots & I_r^s(m,n) \\ \vdots & \vdots & \ddots & \vdots \\ I_r^K(1,1) & I_r^K(1,2) & \cdots & I_r^K(m,n) \end{bmatrix}. \quad (3)$$

Here, $\langle\Phi\rangle = \frac{1}{K}\Sigma_{s=1}^{K}\Phi^s$ represents a $1 \times N$ row vector and I denotes a $K \times 1$ column vector whose elements are all 1. In addition, $B = [B^1 B^2 \cdots B^s \cdots B^K]^T$ denotes a $K \times 1$ column vector and $\langle B\rangle$ represents the ensemble average of B. For the sth measurement, because $B^s = \alpha\Phi^s O$ (Φ^s denotes the sth row vector of the matrix Φ and the object O can be represented as a $N \times 1$ column vector), then $B = \alpha\Phi O$ and Eq. (2) can be further described as

$$O_{\mathrm{GI}} = \frac{\alpha}{K}(\Phi - I\langle\Phi\rangle)^T(\Phi - I\langle\Phi\rangle)O = \frac{\alpha}{K}\Psi^T\Psi O. \quad (4)$$

Here, $\Psi = \Phi - I\langle\Phi\rangle$. From Eq. (4), it is clearly observed that $\Psi^T\Psi$ is an $N \times N$ matrix. In a pseudo-thermal light GI system, when the data in the middle row of the matrix $\Psi^T\Psi$ is plotted by a curve, the number of peaks P above the curve's full-width at half-maximum is in proportion to the speckle's transverse size on the object plane Δr_s (namely $\Delta r_s = P d_{\mathrm{pixel}}$, where d_{pixel} is the transverse pixel size of the camera D_r in the reference path), which determines the spatial transverse resolution of GI. Therefore, in order to improve the spatial imaging resolution, we usually decrease the speckle's transverse size illuminating the object for conventional GI, which makes the matrix $\Psi^T\Psi$ be close to a diagonal matrix.

Pseudo-inverse imaging has been widely applied in the field of signal processing, which has various advantages such as being simpler, faster, and capable of bringing out better reconstructions [22–25]. Instead of Ψ^T, we try to reconstruct the object by computing the intensity correlation between the pseudo-inverse matrix $\Psi^\dagger$ and B. This technique is called PGI, and we try to use Moore–Penrose pseudo-inverse to acquire the pseudo-inverse matrix $\Psi^\dagger$ [23]. According to the former discussion of the GI method, $B = \alpha\Phi O$ in the GI system shown in Fig. 1; then $B - I\langle B\rangle = \alpha(\Phi - I\langle\Phi\rangle)O = \alpha\Psi O$ and PGI can be expressed as

$$O_{\mathrm{PGI}} = \frac{1}{K}\Psi^\dagger(B - I\langle B\rangle) = \frac{\alpha}{K}\Psi^\dagger\Psi O. \quad (5)$$

Based on the character of the pseudo-inverse matrix, because $\Psi^\dagger\Psi$ in Eq. (5) is close to an $N \times N$ scalar matrix as the measurement number K is increased, then $O_{\mathrm{PGI}} \simeq O$, which means that the spatial transverse resolution of PGI is very high and PGI may overcome the limitation of the speckle's transverse size on the object plane to the spatial transverse resolution.

3. EXPERIMENTAL AND SIMULATED RESULTS

To verify the concept, Fig. 2 presents experimental results of five slits (140×72 pixels, with pixel size of 6.0 μm × 6.0 μm) and transmission aperture ("zhong" ring) (100×100 pixels) reconstructed by GI and PGI methods in different measurements K. The width of the five slits is $a = 30$ μm and the height is 250 μm. The center-to-center separation is $d = 60$, 120, 180, and 240 μm, respectively. The diameter of the aperture ("zhong" ring) is 480 μm. The parameters listed in Fig. 1 are set as follows: $z = 200$ mm, $z_1 = 2f = 500$ mm, and $z_2 = 2f_1 = 200$ mm. The effective transmission apertures for the lens f and the lens f_1 are about $L = 2.4$ mm and $L_1 = 20.0$ mm, respectively. In addition, the pixel size of the CCD camera is about 6.0 μm × 6.0 μm, and the exposure time is set to 1 ms. According to the Rayleigh criterion, the speckle's transverse size on the object plane is $\Delta r_s \simeq \frac{1.22\lambda z_1}{L} = 165.2$ μm. By $K = 10,000$ measurements and

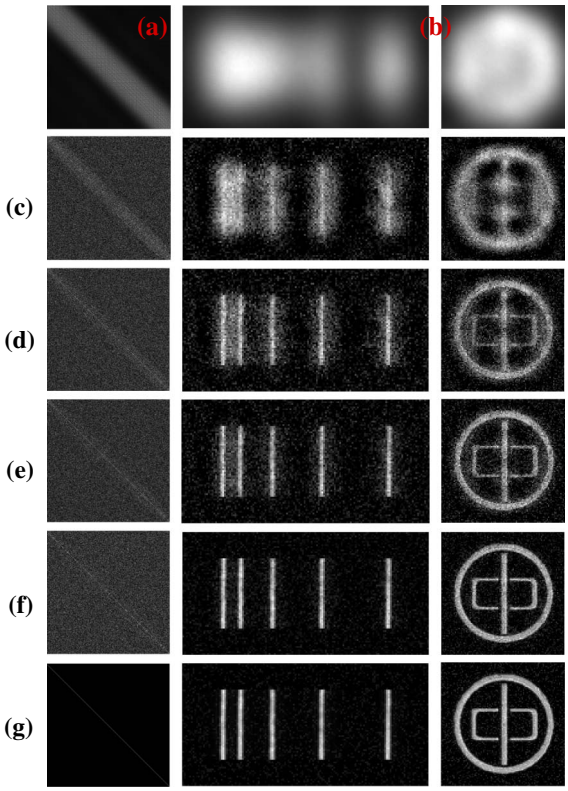

Fig. 2. Results of experimental demonstration of high-resolution PGI. (a) $\Psi^T\Psi$; (b) GI reconstruction results using $K = 10,000$ measurements. Left column of (c)–(g), $\Psi^\dagger\Psi$ in different measurements K; middle column of (c)–(g), five slits reconstructed by PGI method in different measurements K; right column of (c)–(g), transmission aperture ("zhong" ring) recovered by PGI method in different measurements K. (c) $K = 1000$ (the compression ratio $\eta = \frac{K}{N_{\text{pix}}} = 0.1$, namely 10% Nyquist limit); (d) $K = 3000$ ($\eta = 0.3$, namely 30% Nyquist limit); (e) $K = 5000$ ($\eta = 0.5$, namely 50% Nyquist limit); (f) $K = 8000$ ($\eta = 0.8$, namely 80% Nyquist limit); (g) $K = 10,000$ ($\eta = 1.0$, namely 100% Nyquist limit).

choosing the speckle patterns with 100×100 pixels to form a $10,000 \times 10,000$ matrix, the results of $\Psi^T\Psi$ are shown in Fig. 2(a) and the peak number above the distribution's full-width at half-maximum for the middle row of $\Psi^T\Psi$ is $P = 27$; then $\Delta r_s = Pd_{\text{pixel}} \simeq 162.0$ μm, which is in accordance with the result predicted by the Rayleigh criterion. Therefore, as displayed in Fig. 2(b), neither the five slits nor the aperture ("zhong" ring) can be resolved by the GI method. However, using the PGI method, the object's images can be successfully reconstructed [middle column and right column of Figs. 2(c)–2(g)]. Further, as the measurement number K is increased [as shown in the left column of Figs. 2(c)–2(g)], it is clearly observed that $\Psi^\dagger\Psi$ is closer to a scalar matrix and the imaging quality of PGI will be better. In addition, for the objects such as the five slits and the aperture ("zhong" ring), there are about $N_{\text{pix}} = 10,000$ pixels and the reconstruction of such objects requires at least N_{pix} measurements for standard conventional imaging, which sets the measurement's Nyquist limit [8,17]. For PGI, however, as shown in Figs. 2(c)–2(g), the object can only be achieved using the measurement of 30% Nyquist limit.

To validate the applicability of high-resolution PGI for more general images, Fig. 3 gives a numerical experimental

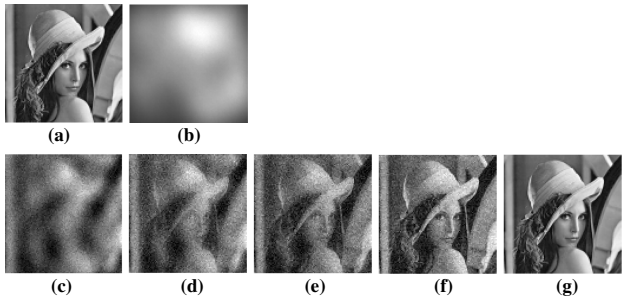

Fig. 3. Numerical experimental demonstration of high-resolution PGI for gray-scale objects. (a) Original object; (b) GI reconstruction result using $K = 10,000$ measurements; (c)–(g) reconstruction results obtained by PGI method with compression ratio $\eta = 0.1$, 0.3, 0.5, 0.8, and 1.0, respectively.

demonstration of imaging a continuously varying gray-scale object, i.e., a slide representing a detail of the famous picture "lena" (100×100 pixels). Using the same experimental parameters as in Fig. 2, the matrix Φ is composed by the intensities recorded by the CCD camera D_r, and the data B is obtained by directly computing ΦO. Based on the GI method described in Eq. (4), the reconstruction result is shown in Fig. 3(b). Figures 3(c)–3(g) illustrate PGI results in a different compression ratio η, which is similar to the experimental results shown in Figs. 2(c)–2(g). Therefore, we demonstrate that PGI can dramatically improve the spatial transverse resolution of GI even using the measurements far below the Nyquist limit.

To measure quantitatively the reconstruction quality of PGI in different η, the reconstruction fidelity is estimated by calculating the peak signal-to-noise ratio (PSNR):

$$\text{PSNR} = 10 \times \log_{10}\left[\frac{(2^p - 1)^2}{\text{MSE}}\right]. \tag{6}$$

Here, the bigger the PSNR value, the better the quality of the recovered image. For a 0–255 gray-scale image, $p = 8$ and MSE represents the mean square error of the reconstruction image O_{PGI} with respect to the original object O, namely

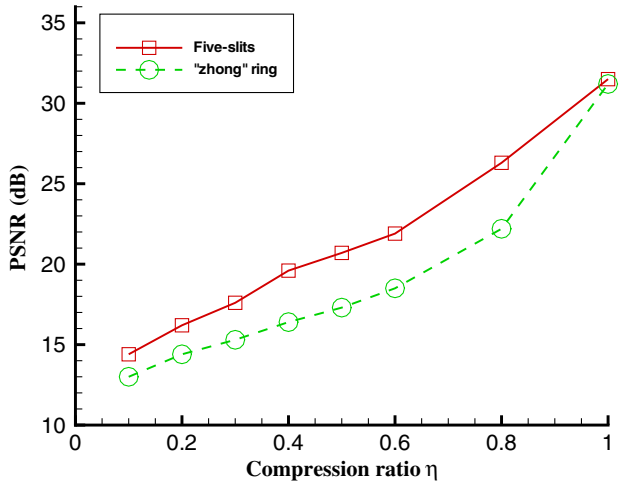

Fig. 4. Performance between PSNR and compression ratio η based on the results obtained in Fig. 2. Solid curve with red squares shows PGI reconstruction results of five slits and dashed curve with green circles corresponds to PGI reconstruction results of the transmission aperture ("zhong" ring).

$$\mathrm{MSE} = \frac{1}{N_{\mathrm{pix}}} \sum_{i,j} [O_{\mathrm{PGI}}(x_i, y_j) - O(x_i, y_j)]^2. \quad (7)$$

The dependence of PSNR on η for the five slits and transmission aperture ("zhong" ring) is shown in Fig. 4. It is obviously seen that all curves increase with the compression ratio η, which is also consistent with the results indicated in Fig. 2.

4. CONCLUSION

In conclusion, we have presented a PGI technique that enhances dramatically the spatial transverse resolution of the GI protocol even when using measurements far below the Nyquist limit. We also show that the technique is effective for imaging realistic gray-scale objects. This technique will pave the way for the use of GI in many sensing or imaging problems, such as imaging in the wavebands without cameras, and in optically harsh environments, remote sensing, microscopy in biology, and material and medical sciences.

ACKNOWLEDGMENT

This work was supported by the Hi-Tech Research and Development Program of China under Grant Project No. 2013AA122901, and the Youth Innovation Promotion Association CAS.

REFERENCES

1. A. Gatti, E. Brambilla, M. Bache, and L. A. Lugiato, "Ghost imaging with thermal light: comparing entanglement and classical correlation," Phys. Rev. Lett. **93**, 093602 (2004).
2. R. S. Bennink, S. J. Bentley, R. W. Boyd, and J. C. Howell, "Quantum and classical coincidence imaging," Phys. Rev. Lett. **92**, 033601 (2004).
3. D. Z. Cao, J. Xiong, and K. Wang, "Geometrical optics in correlated imaging systems," Phys. Rev. A **71**, 013801 (2005).
4. D. Zhang, Y.-H. Zhai, L.-A. Wu, and X.-H. Chen, "Correlated two-photon imaging with true thermal light," Opt. Lett. **30**, 2354–2356 (2005).
5. F. Ferri, D. Magatti, A. Gatti, M. Bache, E. Brambilla, and L. A. Lugiato, "High-resolution ghost image and ghost diffraction experiments with thermal light," Phys. Rev. Lett. **94**, 183602 (2005).
6. M. D. Angelo and Y. H. Shih, "Quantum imaging," Laser Phys. Lett. **2**, 567–596 (2005).
7. W. Gong, P. Zhang, X. Shen, and S. Han, "Ghost 'pinhole' imaging in Fraunhofer region," Appl. Phys. Lett. **95**, 071110 (2009).
8. O. Katz, Y. Bromberg, and Y. Silberberg, "Compressive ghost imaging," Appl. Phys. Lett. **95**, 131110 (2009).
9. W. Gong and S. Han, "A method to improve the visibility of ghost images obtained by thermal light," Phys. Lett. A. **374**, 1005–1008 (2010).
10. J. H. Shapiro and R. W. Boyd, "The physics of ghost imaging," Quantum Inf. Process. **11**, 949–993 (2012).
11. N. Tian, Q. Guo, A. Wang, D. Xu, and L. Fu, "Fluorescence ghost imaging with pseudothermal light," Opt. Lett. **36**, 3302–3304 (2011).
12. W. Gong and S. Han, "Correlated imaging in scattering media," Opt. Lett. **36**, 394–396 (2011).
13. J. Bertolotti, E. G. van Putten, C. Blum, A. Lagendijk, W. L. Vos, and A. P. Mosk, "Non-invasive imaging through opaque scattering layers," Nature **491**, 232–234 (2012).
14. C. Zhao, W. Gong, M. Chen, E. Li, H. Wang, W. Xu, and S. Han, "Ghost imaging lidar via sparsity constraints," Appl. Phys. Lett. **101**, 141123 (2012).
15. W. Gong, C. Zhao, J. Jiao, E. Li, M. Chen, H. Wang, W. Xu, and S. Han, "Three-dimensional ghost imaging ladar," arXiv: 1301.5767 (2013).
16. P. Zerom, K. W. C. Chan, J. C. Howell, and R. W. Boyd, "Entangled-photon compressive ghost imaging," Phys. Rev. A **84**, 061804 (2011).
17. J. Du, W. Gong, and S. Han, "The influence of sparsity property of images on ghost imaging with thermal light," Opt. Lett. **37**, 1067–1069 (2012).
18. P. Clemente, V. Durán, V. Torres-Company, E. Tajahuerce, and J. Lancis, "Optical encryption based on computational ghost imaging," Opt. Lett. **35**, 2391–2393 (2010).
19. S. Li, X. Yao, W. Yu, L. Wu, and G. Zhai, "High-speed secure key distribution over an optical network based on computational correlation imaging," Opt. Lett. **38**, 2144–2146 (2013).
20. W. Gong and S. Han, "Experimental investigation of the quality of lensless super-resolution ghost imaging via sparsity constraints," Phys. Lett. A **376**, 1519–1522 (2012).
21. W. Gong and S. Han, "High-resolution far-field ghost imaging via sparsity constraint," Sci. Rep. **5**, 9280 (2015).
22. C. Zhang, S. Guo, J. Cao, J. Guan, and F. Gao, "Object reconstitution using pseudo-inverse for ghost imaging," Opt. Express **22**, 30063–30073 (2014).
23. S. Chountasis, V. N. Katsikis, and D. Pappas, "Digital image reconstruction in the spectral domain utilizing the Moore-Penrose inverse," Math. Prob. Eng. **2010**, 750352 (2010).
24. R. Barankov and J. Mertz, "High-throughput imaging of self-luminous objects through a single optical fibre," Nat. Commun. **5**, 5581 (2014).
25. S. M. Kolenderska, O. Katz, M. Fink, and S. Gigan, "Scanning-free imaging through a single fiber by random spatio-spectral encoding," Opt. Lett. **40**, 534–537 (2015).